

# The Variational Power of Quantum Circuit Tensor Networks

Reza Haghshenas,<sup>1,\*</sup> Johnnie Gray,<sup>1,†</sup> Andrew C. Potter,<sup>2,3</sup> and Garnet Kin-Lic Chan<sup>1,‡</sup>

<sup>1</sup>*Division of Chemistry and Chemical Engineering, California Institute of Technology, Pasadena, California 91125, USA*

<sup>2</sup>*Department of Physics, University of Texas at Austin, Austin, TX 78712, USA*

<sup>3</sup>*Department of Physics and Astronomy, and Quantum Matter Institute, University of British Columbia, Vancouver, BC, Canada V6T 1Z1*

We characterize the variational power of quantum circuit tensor networks in the representation of physical many-body ground-states. Such tensor networks are formed by replacing the dense block unitaries and isometries in standard tensor networks by local quantum circuits. We explore both quantum circuit matrix product states and the quantum circuit multi-scale entanglement renormalization ansatz, and introduce an adaptive method to optimize the resulting circuits to high fidelity with more than  $10^4$  parameters. We benchmark their expressiveness against standard tensor networks, as well as other common circuit architectures, for both the energy and correlation functions of the 1D Heisenberg and Fermi-Hubbard models in the gapless regime. We find quantum circuit tensor networks to be substantially more expressive than other quantum circuits for these problems, and that they can even be more compact than standard tensor networks. Extrapolating to circuit depths which can no longer be emulated classically, this suggests a region of quantum advantage with respect to expressiveness in the representation of physical ground-states.

## I. INTRODUCTION

Advances in digital quantum computing have led to renewed interest in quantum circuit representations of many-body states. For this purpose, it is crucial to understand the representational power and trainability of different circuit architectures. Out of the many possible architectures, one promising choice are circuits derived from tensor network states used in classical simulations of quantum states with limited entanglement. Because of the close connections between tensor networks and quantum circuits, and the significant numerical experience using them in classical simulations, they provide a natural setting to define the boundary between classical and quantum capabilities for quantum simulation. The simplest measure of the classical complexity of a tensor network is the tensor bond dimension. Consequently, one can construct a tensor network that is hard to simulate classically by devising a quantum circuit that maps to a tensor network with a very large bond dimension, in a small number of circuit elements. For example, one can construct quantum circuits that generate tensors with bond dimensions exponential in the circuit depth. This is the idea behind “deep” or quantum circuit tensor networks which have been of interest for different applications of quantum devices<sup>1–6</sup>. Further, when combined with mid-circuit measurements and qubit reuse, some of these methods allow simulation of large-scale quantum systems with few physical qubits<sup>4,7,8</sup>.

However, constructing a class of states that is hard to represent classically is not sufficient to advance the simulation of physical systems. In the context of physical quantum many-body states, we must address additional questions (i) are sparsely parameterized quantum “circuit” tensor networks capable of representing physical states more efficiently than the “dense” tensor networks traditionally used in classical simulation? (ii) and for this task, what are the optimal circuit architectures and optimization protocols? The answers have potential implications not only for quantum simulations, but also for classical simulations with tensor networks. For example an affirmative answer to (i) would suggest that it may

sometimes be better to classically simulate with the quantum circuit tensor network directly, rather than via the classical dense tensor network, so long as the circuit depth and tensor values support efficient classical contraction and/or approximation.

Some work to answer questions (i) and (ii) has already appeared, such as in Refs<sup>9–12</sup>. In this work, our focus will be on establishing the variational power of quantum tensor networks to capture quantum many-body ground-states. This is an application where traditional dense tensor networks do well, and is thus in some sense the hardest test for quantum circuit tensor networks to pass. We will focus in particular on understanding the resources (e.g. number of variational parameters) required, optimization strategies, and influence of circuit architecture on the results. Because of the large number of numerical experiments required, we will limit ourselves to one-dimensional quantum many-body states, although we expect analogous findings to extend to simulations in higher dimensions. As we shall demonstrate, with careful optimization strategies, quantum circuit tensor networks are very expressive, and in some cases, even more expressive than classical dense tensor networks. This suggests a regime where a quantum advantage in expressiveness may be observed in physical ground-state simulations.

The structure of the paper is as follows. We first introduce quantum circuit tensor networks, review the mapping between two common tensor networks, the matrix product state and the multiscale entanglement renormalization ansatz<sup>13</sup> (MERA), to block unitary circuits<sup>4,6</sup>, and introduce different architectures for the local unitary representations. We then examine optimization strategies for such circuits. Finally, we carry out a detailed comparison between the quantum circuit tensor networks, classical dense tensor networks, and reference circuit classes studied in the literature, to evaluate their variational efficiency and power, for both energies and correlation functions.

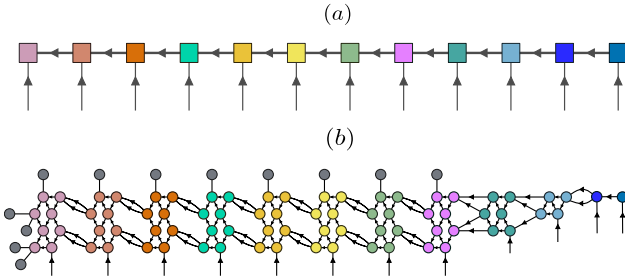
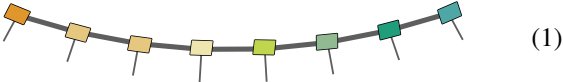


FIG. 1. (Color online) Schematic representation of a matrix product state and its quantum circuit in (a) right canonical form for a system with  $L = 12$  (or equivalently 12 qubits). (b) A quantum circuit MPS with four bond qubits ( $q = 4$ ) and a local brickwall circuit structure with depth  $\tau = 4$ . The square tensors  $\square$  represent isometric tensors, while the circle tensors  $\circ$  are two-qubit unitary gates. The black tensors denote register qubits initialized in the  $|0\rangle$  state. Note that the arrows associated with the MPS and quantum circuit MPS follow the tensor network convention rather than the circuit convention, i.e. they are in the opposite direction of circuit-execution time.

## II. TENSOR NETWORKS AND QUANTUM CIRCUITS

### A. The Canonical Form of the Matrix Product State

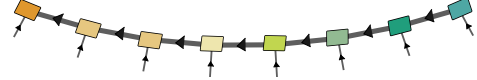
A matrix product state (MPS)<sup>14–16</sup> is a tensor network consisting of a tensor for each site, connected by bonds in a one-dimensional geometry. It is represented diagrammatically by



where each square tensor  $\square$  denotes a  $D \times D \times d$ -dimensional tensor. The open bonds index the  $d$ -dimensional physical Hilbert space of the site. (For example, if  $d = 2$ , we can identify each site with a qubit). The connected “virtual” bonds of dimension  $D$  then control the number of parameters and thus the variational power of the MPS (or more physically, the maximum bipartite entanglement at each bipartition in the network).

The individual tensors in an MPS are not in unique correspondence with a given quantum state due to gauge degrees of freedom: the state is invariant under insertion of a gauge matrix and its inverse  $G, G^{-1}$  between two tensors (along a virtual bond). To fix the gauge degrees of freedom, a MPS can be recast into a canonical form<sup>17</sup>. In canonical form, the tensors satisfy additional isometric or normalization constraints, but for a (normalized) MPS, this imposes no loss of representational power. A simple algorithm to obtain the canonical form is to perform a sequence of  $QR$  ( $LQ$ ) decompositions of the tensors; doing this from left to right (right to left) brings an arbitrary MPS into left (right) canonical form<sup>18</sup>. For example, the right canonical form of the MPS in Eq. 1 can be

represented by the following diagram:



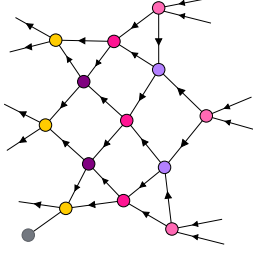
where every square tensor with arrows  $\square$  is an isometric tensor. The isometric condition is satisfied for contractions performed on the incoming bonds  $\square$ , where the left side of the equality is the identity matrix. The isometric constraint fixes the gauge freedom up to permutations of bond indices. In a similar way, the right canonical form is defined by tensors which satisfy an isometric condition  $\square = \square$ , while a “mixed canonical form” (central to the density matrix renormalization group (DMRG)<sup>19</sup>) is obtained by combining left and right canonical forms around a given central site, with the central tensor satisfying the condition  $\square = 1$ . When the tensors in a canonical MPS satisfy isometric conditions, the MPS is an example of an “isometric” tensor network<sup>20,21</sup>. The number of independent variational parameters in a canonical MPS of length  $L$ , with all elements real, scales asymptotically as  $\sim L \times D(3D - 1)/2$ . We will refer to these standard MPS as “dense” MPS (dMPS). Because of the close relationship between the standard MPS formulation and the DMRG, we will sometimes use the term DMRG.

### B. Quantum circuit MPS

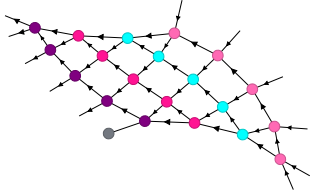
Given the canonical form of the MPS, the mapping to a block unitary quantum circuit follows a simple procedure<sup>4,6,22</sup>. This is because isometric tensors can be viewed as arising from the application of a unitary tensor to a partial set of inputs. Concretely, the steps are as follows: (i) The virtual bonds of dimension  $D$  (thick lines) are viewed as  $q$  qubit bonds (aggregate dimension  $D = 2^q$ ) (thin lines). Graphically, this is the relation  $\square = \square$ . (Note that, following standard MPS conventions, the arrows on these diagrams indicate right-canonical form, and are opposite to the execution-time direction in the associated quantum circuit). (ii) The isometric tensors are viewed as columns of a block unitary matrix with one fixed output qubit (denoted by a black dot), i.e.  $\square = \square$ . This mapping generates the MPS via a block unitary circuit, where each block unitary is a matrix of dimension  $dD \times dD$ .

In the above mapping, the variational space of normalized states generated by the block unitary circuit and the standard “dense MPS” (dMPS) are exactly the same. However, we can imagine replacing the block unitary by a local circuit of two-qubit gates of given depth. One can then create a block unitary that acts on a set of  $q$  qubits, using as few as  $O(q)$  two-qubit gates. This allows us to generate an entangled state that lives in the variational space of a  $D = 2^q$  dMPS, with only  $O(q)$  variational parameters per site. We refer to an MPS where the block unitary is encoded as a local circuit as a “quantum circuit MPS” (qMPS).

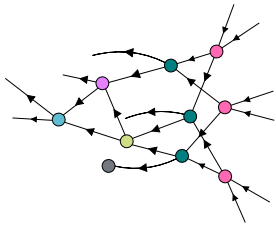
There is much freedom to choose the structure of the local circuit. Here, we explore several local circuit structures: (i) a brick-wall circuit, denoted graphically as



with densely connected nearest-neighbour two-body unitary gates (circle tensors  $\circlearrowleft$ ). Throughout, colors visually distinguish different circuit layers, but each gate of a given color implements a distinct gate. For the brick-wall circuit, we refer to a layer of even gates and a layer of odd gates as two layers, thus the above circuit has a circuit depth of  $\tau = 6$ . In a brick-wall circuit, correlations spread slowly with increasing  $\tau$ , as the effective correlation length  $\xi$  grows linearly with circuit depth  $\xi \sim \tau$ . (ii) A ladder circuit, for example,



where we label the circuit above as depth  $\tau = 4$ . Correlations propagate more efficiently in this structure: with  $\tau = 1$ , the first and last qubits are already correlated. (iii) A MERA structure



which represents a binary MERA<sup>23</sup> with depth  $\tau = 5$ . Properties of MERA circuits in general are discussed more in the section below. Note that here, however, the MERA structure is only being used for the local circuit (i.e. a MERA quantum circuit, rather than a quantum circuit MERA) and globally, the ansatz is still a qMPS. An example of the final circuit structure of the qMPS using a local brick-wall circuit is shown in Fig. 1. Corresponding figures for qMPS with local ladder and MERA circuits are shown in Fig. 9.

Overall, the variational power of the qMPS ansatz is determined by three factors: (i) number of qubits  $q$  on which each block unitary circuit acts (placing the qMPS in the variational space of a dense MPS with  $D = 2^q$ ), (ii) the number of gates in the local circuit, (iii) the internal structure of the local circuit. Note that the number of gates in each layer differs between the local circuit structures, thus  $\tau$  should not be

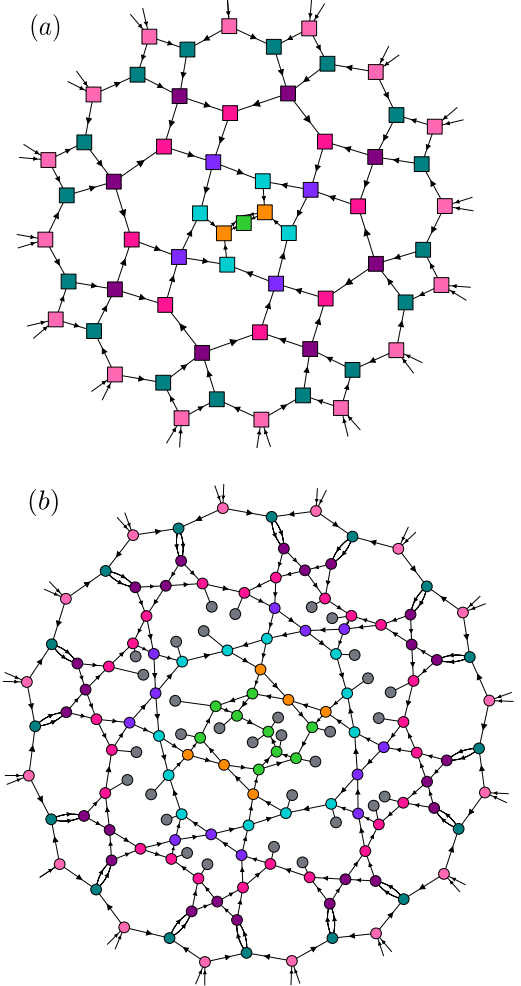


FIG. 2. (Color online) (a) A binary MERA wave function for  $L = 32$  qubits, and (b) its quantum circuit, i.e. qMERA, where the local quantum circuit is chosen to have a brick-wall structure with  $q = 2$  and  $\tau = 2$ . The different layers of the MERA are shown in different colors.

directly compared between the different structures. Instead, the number of gates (or equivalently, variational parameters) asymptotically behaves as  $\sim \frac{1}{2}\tau L(q + 1)$ ,  $\sim \tau L(q + 1)$  and  $\sim 2\tau L(q + 1)$  for the brick-wall, ladder, and MERA structures, respectively. In the numerical simulations, we will refer to these three kinds of qMPS circuits as qMPS-b, qMPS-l, and qMPS-m, respectively.

### C. Quantum circuit MERA

Another commonly used tensor network state is the MERA. This is a tensor network state where the tensors are arranged to introduce bipartite entanglement at multiple scales. In this ansatz, isometric tensors perform coarse-graining while unitary disentanglers are applied to remove short-range entanglement at the different length scales. We show a binary form

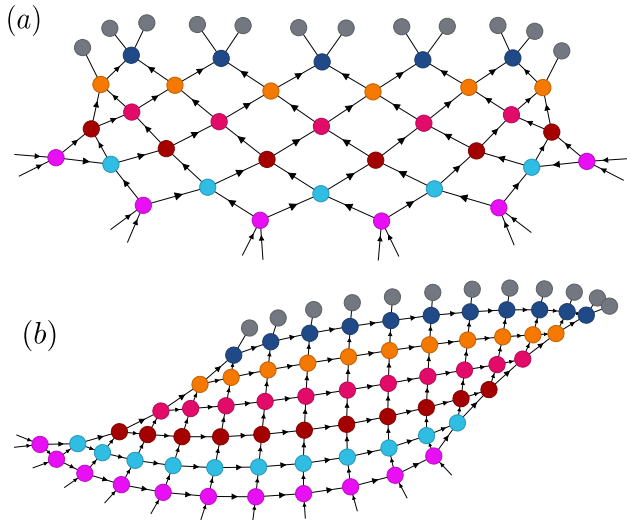


FIG. 3. (Color online) Global quantum circuits with (a) brick-wall and (b) ladder structures.

of MERA in Fig. 2(a) with unitary disentanglers and isometric coarse-graining tensors  $\square$  distinguished by different colors in each layer. We will refer to the standard form of MERA where all tensors are assumed dense as dense MERA (dMERA).

Since MERAs are isometric tensor networks by construction, like in the MPS canonical form, a quantum circuit MERA (i.e. a circuit whose global structure is derived from the MERA) i.e. qMERA can be straightforwardly obtained by decomposing both the block isometric and unitary tensors into local circuits with a finite depth  $\tau$  and given internal structure as already discussed. A graphical illustration of a qMERA is shown in Fig. 2(b). An important difference between a qMERA and a qMPS is the presence of a structured set of long-range unitary gates. In 1D, this allows the qMERA to capture critical entanglement beyond the area law with only a polynomial number of gates<sup>24</sup>.

Similarly to the qMPS, the accuracy of the qMERA ansatz is determined by three factors, i.e.  $q$ , the number of gates, and the internal structure of local circuits. In this work, we only consider qMERA with local brick-wall circuits as depicted in Fig. 2(b)<sup>25</sup>, which we will refer to as qMERA-b in the numerical studies.

#### D. Global quantum circuit ansatz

To place the performance of the quantum circuit tensor networks in context, we also consider global brick-wall and ladder circuit ansätze, as depicted in Fig. 3. These are referred to as QC-b and QC-l in the numerical studies below. As discussed above, the brick-wall is less efficient than the ladder circuit at spreading correlations among the qubits. Note, however, that although the ladder circuit spreads correlations ef-

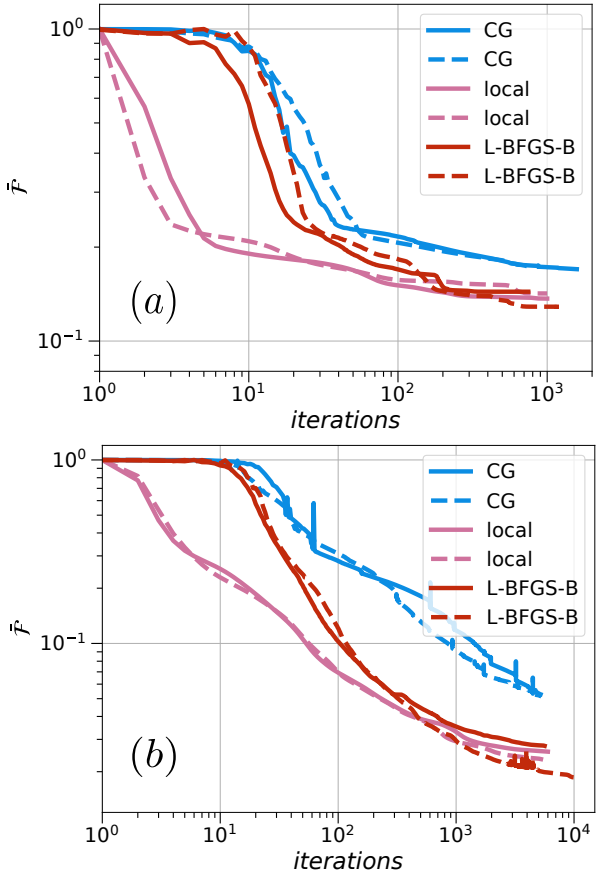


FIG. 4. (Color online) The influence of the choice of optimization method. (a) The infidelity  $\bar{F}$  versus iteration number for the global brick-wall ansatz QC-b with  $L = 16, \tau = 6$ , optimized by CG, L-BFGS-B and local methods. The solid and dashed lines represent two different initial starting states, chosen from a uniform random distribution for the tensors. (b) The same plot for a qMPS-b with  $L = 24, q = 4, \tau = 4$ . The targeted wave function is the ground state of Heisenberg model  $\mathcal{H}_H$ .

ficiently, in contrast to qMERA, using a similar number of gates does not capture the critical logarithmic corrections to the entanglement that characterizes 1D gapless ground-states.

### III. NUMERICAL OPTIMIZATION STUDIES

#### A. Algorithms

The first question to answer when considering the variational power of an ansatz is how to optimize it. In this section, we investigate how to optimize the quantum circuit tensor network and global circuit ansatz considered in this work, by optimizing the parameters of the two-body unitary gates  $\otimes$ . We assume each two-body unitary is a general  $SO(4)$  unitary (i.e. real-valued unitary) with a 6 dimensional variational space<sup>26</sup>. We use two optimization algorithms: (i) a local “DMRG”-like optimization, where we sweep through

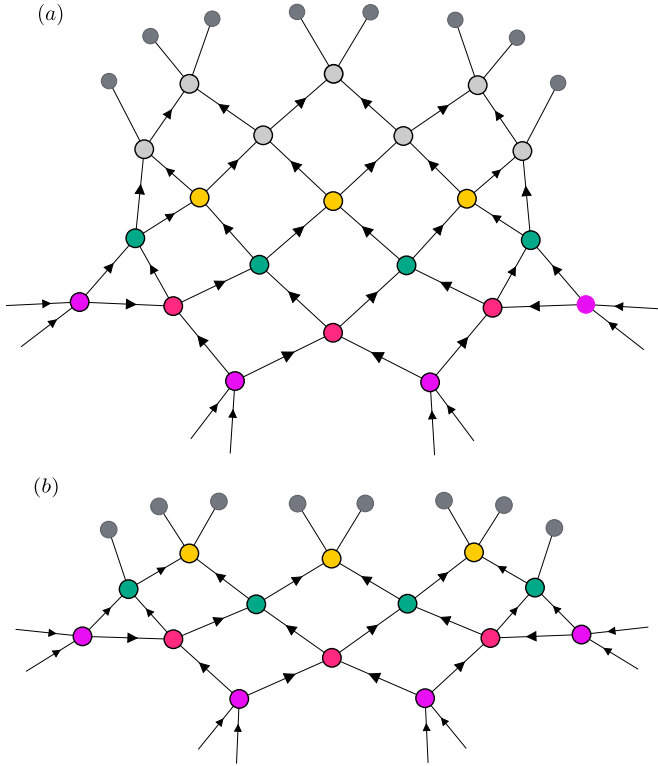


FIG. 5. (Color online) Adaptive initialization of a QC-b circuit with (a)  $\tau = 6$  from an optimized smaller circuit (b) with  $\tau = 4$ . The gates  $\otimes$  denote identity operators with some small random perturbations.

the unitary gates  $\otimes$ , optimizing them one at a time while holding the others fixed; (ii) a global gradient-based optimization, where all variational parameters are updated at the same time. In the local optimization scheme, a linearization of the problem, similar to the one used in MERA optimizations<sup>23</sup>, is used to find locally optimal gates. In the global gradient-based scheme, the global gradient (i.e. the first-order derivative with respect to all variational parameters  $\partial(\dots, \otimes, \otimes, \dots)$ ) is analytically calculated by automatic differentiation as supported in `quimb`<sup>27</sup>. The energy is computed via exact contraction<sup>28</sup> of either a matrix product operator representation of the Hamiltonian (MPS) or a sum of local terms (MERA). The unitary constraints are enforced by differentiating through a function that maps the gate parameters to a unitary matrix. The cost-function minimization is then performed using either Conjugate Gradient (CG) or Limited-Memory Broyden–Fletcher–Goldfarb–Shanno (L-BFGS-B) algorithms<sup>29,30</sup>.

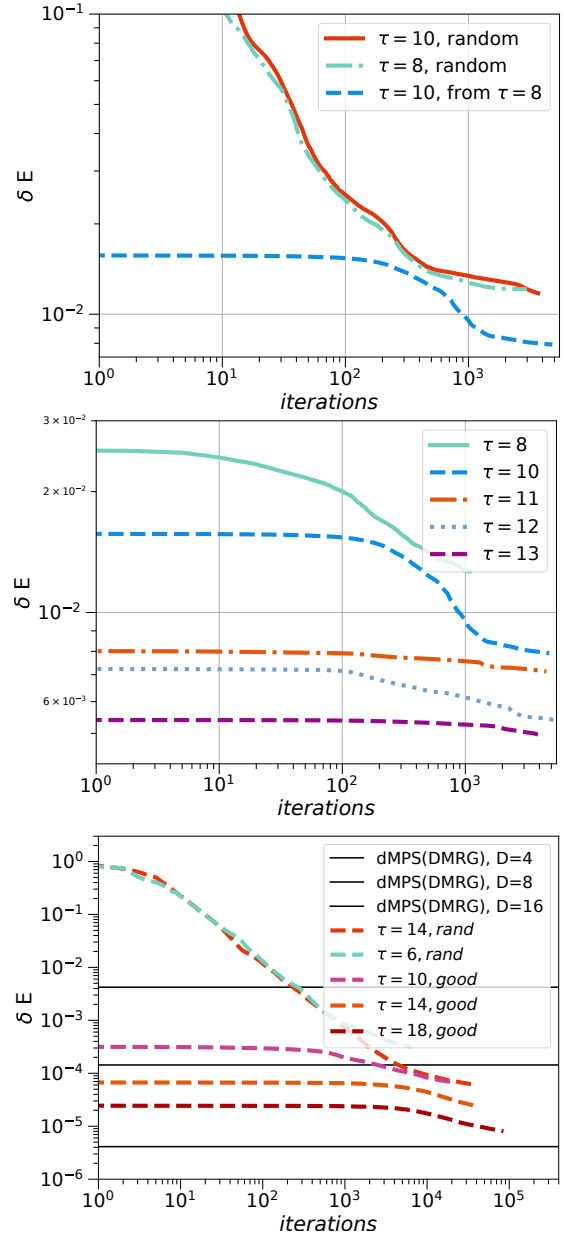


FIG. 6. (Color online) The role of the initial guess in the optimization. (a) The relative error of the ground-state energy  $\delta E$  (of Heisenberg model  $\mathcal{H}_H$ ) as a function of iteration number for a global brick-wall quantum circuit (QC-b) with depth  $\tau$ . When the  $\tau = 10$  ansatz is initialized from the optimized  $\tau = 8$  parameters, we obtain a better minimum than from a random initial guess. Notice that when using a random initial guess the ansatz optimization can get stuck in a poor minimum, as seen by the  $\tau = 8$  (random) and  $\tau = 10$  (random) results, which obtain the same minimum. (b) A better initialization procedure using optimized circuit parameters from smaller depths guarantees that the relative error decreases monotonically when increasing circuit depth  $\tau$ . (c) Similar plot for a qMPS ansatz with  $q = 4$ . We similarly find the relative error drops monotonically when increasing  $\tau$  using initial guesses from a smaller  $\tau$  ansatz (good), while initializing from random guesses (rand) results in optimizations which terminate at poor minima. Reference data from dense MPS (DMRG) also shown.

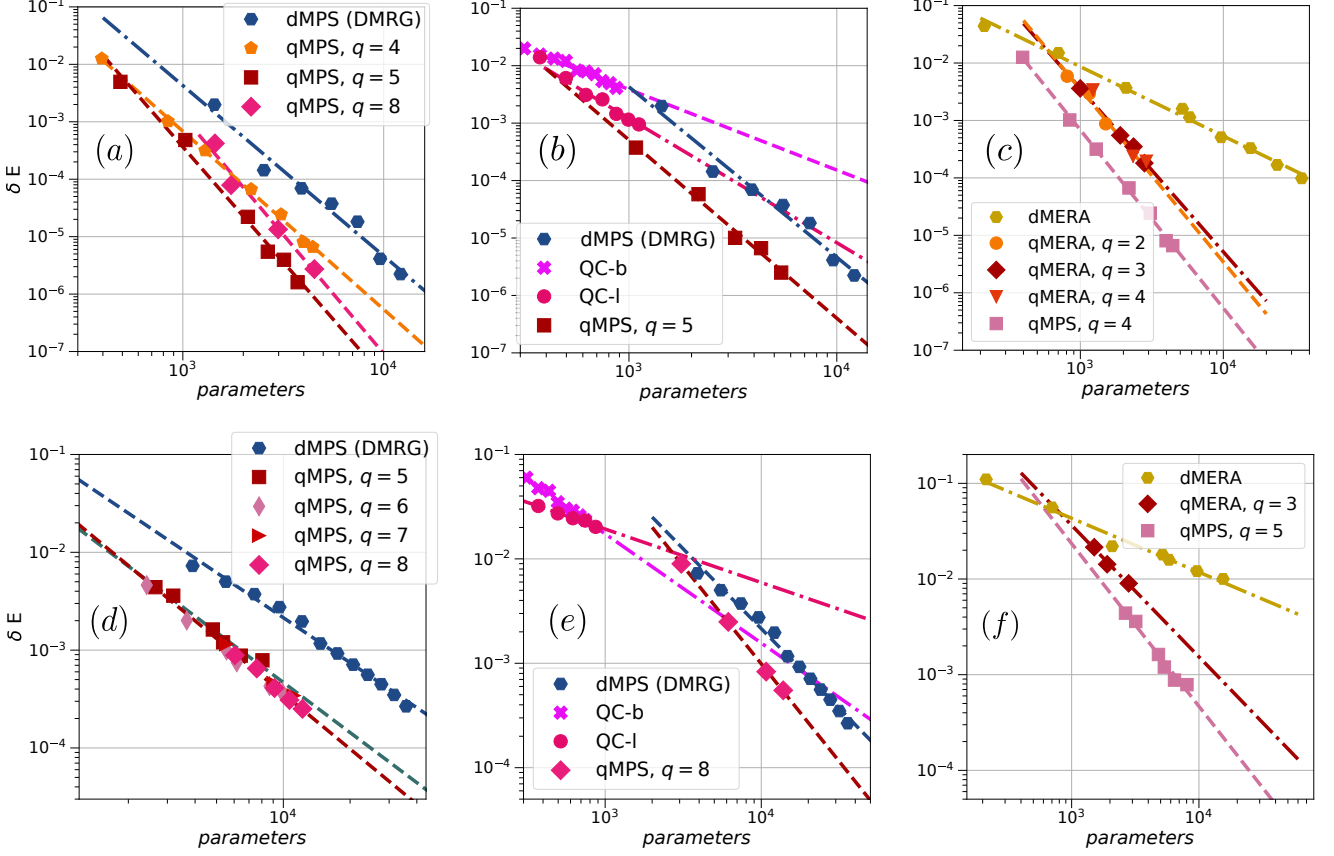


FIG. 7. (Color online) Comparing the variational power of quantum circuit tensor networks (qMPS, qMERA), dense tensor networks (dMPS and dMERA), and global quantum circuits (QC). We show the relative energy error  $\delta E$  versus the number of variational parameters in the ansatz for the Heisenberg (a,b,c) and Fermi-Hubbard (d, e, f) models with  $L = 32$ . Indices 'b' and 'l' stand for brick-wall and ladder. (a, b) Comparison between qMPS with local brick-wall and ladder circuits with DMRG and QC with brick-wall and ladder structures. The largest circuit depth used for QC-b(l) and qMPS-b(l) with  $q = 5$  is  $\tau = 14(9)$ . (c) The performance of qMERA-b versus qMPS and dMERA. The largest parameter sets used for the qMERA-b ansatz correspond to  $q = 4, \tau = 8$ . (d, e, f) The same comparison for the Fermi-Hubbard model. The largest circuit depths for qMPS-b with  $q = 8$  and qMERA-b with  $q = 3$  are  $\tau = 32$  and  $\tau = 12$ , respectively.

## B. Model Hamiltonians

We choose to study the 1D Heisenberg and Fermi-Hubbard models:

$$\begin{aligned} \mathcal{H}_H &= J \sum_i \vec{S}_i \cdot \vec{S}_{i+1}, \\ \mathcal{H}_{FH} &= -t \sum_{i,\sigma} \left( c_{i\sigma}^\dagger c_{i+1\sigma} + h.c. \right) + U \sum_i c_{i\uparrow}^\dagger c_{i\uparrow} c_{i\downarrow}^\dagger c_{i\downarrow} - \\ &\quad - \mu \sum_{i\sigma} c_{i\sigma}^\dagger c_{i\sigma}, \end{aligned}$$

where  $\vec{S}$  are spin-1/2 operators and  $c_\sigma^\dagger, c_\sigma$  are spin-1/2 fermionic creation and annihilation operators respectively. For the Heisenberg model we use  $J = 1$ , and for the Hubbard model we use  $t = 1, U = 3$  and  $\mu = U/10$ . In both cases, the ground states are gapless in the thermodynamic limit with algebraically decaying correlation functions.

## C. Local Optimization versus Global Optimization

We first compare local ‘‘DMRG’’ style optimization versus global gradient-based optimization for the infidelity cost function  $\bar{\mathcal{F}} = 1 - |\langle \Psi | \psi \rangle|$ , where  $|\Psi\rangle$  is the ground-state wavefunction of the model and  $|\psi\rangle$  is the ansatz state.  $|\Psi\rangle$  is obtained by the standard DMRG algorithm using a dense MPS of sufficiently large bond dimension ( $D \sim 400$ ) so that any error in  $|\Psi\rangle$  is negligible. When  $\bar{\mathcal{F}} = 0$  then the circuit ansatz is identical to the ground-state wave function.

The result of minimizing  $\bar{\mathcal{F}}$  for the different ansatz and optimization methods is shown in Fig. 4. We show data from the quantum circuit MPS with a brick-wall local ansatz (qMPS-b) ( $L = 24, q = 4, \tau = 6$ ) and global brick-wall quantum circuit (QC-b) ( $L = 16, \tau = 6$ ) as representative examples. We find that in all cases, the local DMRG style optimization converges to the local minimum faster than the global gradient-based optimization using either the CG or L-BFGS-B algorithms. In addition, we find that in all cases, the L-BFGS-B algorithm

converges more quickly than the CG algorithm. However, we also see that both the speed of convergence as well as the final converged result has some dependence on the initial guess. As observed in Fig. 4, given a suitable initial guess, the global gradient-based optimization eventually converges to a slightly lower minimum than that found by the local DMRG optimization.

#### D. Initial Guess

The dependence of the optimization on the initial guess is well-known in quantum circuit optimization, where poor initial guesses can sometimes give rise to exponentially small gradients (the barren plateau problem<sup>31–35</sup>). We can see a related problem in our circuits. To illustrate this, we show results from optimizing the energy cost function  $E = \min \langle \psi | \mathcal{H} | \psi \rangle$ ,  $|\psi\rangle \in \text{qTN}$  and we report the relative energy error  $\delta E = E/E_{\text{exact}} - 1$  versus iteration number in Fig. 6 for several example circuits. We see in the top panel (Fig. 6(a)) that when starting from a random initial guess for the global QC-b ansatz, we converge to the same relative error for two different circuit depths  $\tau = 8$  and  $\tau = 10$ , despite the significantly larger number of variational parameters for  $\tau = 10$  versus  $\tau = 8$ .

To improve the initialization of larger circuits, we use optimized gates obtained from a shallow circuit to initialize gates at larger circuit depth. The heuristic for this adaptive initialization method is summarized as follows: (i) optimal gates are obtained from a random initial guess for a low depth circuit  $\tau'$ , (ii) the initial guess for the ansatz with depth  $\tau > \tau'$ , is given by the optimized gates (from previous calculations) for  $\tau \geq \tau'$  and the identity operator for  $\tau < \tau'$ , respectively (measuring depth from the register qubits) (see Fig. 5 for an explicit example), (iii) small random perturbations to all gates in the ansatz are applied to avoid getting stuck in a local minimum, (iv) for a circuit ansatz with larger depth, we repeat steps (ii, iii). Empirically, it is found that a gradual increase of the circuit depth by 2–6 layers works well, i.e.  $\tau - \tau' = 2–6$ . The identity perturbation strength is also chosen to be of the same order as the local unitary gradient norm.

In Fig. 6(a), we show that optimizing the global QC-b ansatz with  $\tau = 10$  starting from optimal gates from  $\tau = 8$ , indeed results in a lower relative error. In Fig. 6(b), we plot the results of optimizing the QC-b ansatz with different  $\tau$  (each initialized in the manner above, using lower depth circuits as shown in Fig. 5(c)), which shows that we can now achieve a systematic decrease in the relative error  $\delta E$  as function of increasing  $\tau$ . Notice that in all cases, it is necessary to use many iterations to bring the ansatz out of the local minimum generated by the smaller  $\tau$  guess, before one observes a significant drop in the relative error. Similar results are shown for the qMPS-b ansatz with fixed  $q = 4$  and increasing  $\tau$  for the local circuit (brick-wall ansatz) in Fig. 6(c); we similarly see that we can achieve a systematic decrease in the relative error when increasing  $\tau$ . Indeed, as we increase  $\tau$  in the qMPS-b ansatz, we obtain results that approach the dense MPS (DMRG) result with bond dimension  $D = 2^q = 16$ .

Ansatz	Heisenberg, $(a, b)$	Hubbard, $(a, b)$
qMPS-b	(20, 4.0)	(9, 1.9)
qMPS-l	(14, 3.1)	(10, 1.9)
QC-b	(4, 1.4)	(4.4, 1.0)
QC-l	(8, 2.2)	(0.4, 0.5)
qMERA-b	(15, 3.1)	(6.0, 1.4)
dMPS (DMRG)	(15, 2.9)	(8.0, 1.5)
dMERA	(3.5, 1.2)	(0.8, 0.6)

TABLE I. Scaling coefficients  $(a, b)$  in the form  $\delta E \sim an^{-b}$  for the various ansatz in the Heisenberg and Fermi-Hubbard models. The asymptotic behaviour of the relative error  $\delta E$  at large  $n$  is controlled by  $b$ .

As this is the lower bound for the variational energy of any qMPS with  $q = 4$ , our optimization heuristic using adaptive initialization thus fully realizes the variational power of the quantum circuit tensor network.

## IV. VARIATIONAL POWER OF QUANTUM CIRCUIT TENSOR NETWORKS, DENSE TENSOR NETWORKS, AND GLOBAL QUANTUM CIRCUITS

### A. Energies

Using the above optimization strategies, we can now systematically characterize the variational power of the different ansätze discussed in this work for ground-state representation. As the measure of expressiveness, we use the relative energy error  $\delta E$  as a function of the number of variational parameters. (Related measures have been recently used to compare different variational wavefunctions<sup>36</sup>). The various ansatz are optimized using the global gradient scheme with the L-BFGS-B algorithm, while the dense MPS results are obtained by the DMRG algorithm. The largest parametrized circuit ansätze correspond to the following: (i) for qMPS-b and qMERA-b, the number of bond qubits and local circuit depths are  $q = 8, \tau = 32$  and  $q = 4, \tau = 8$  respectively, and (ii) for the global circuit ansatz QC-b and QC-l, the largest circuit depths are  $\tau = 14$  and  $\tau = 9$  respectively. Despite the large number of circuit parameters, we find that the optimization heuristics work to high accuracy, if sufficient iterations are used. For example, the smallest relative energy errors we find using the qMPS ansatz are  $10^{-6}$  and  $10^{-4}$  for the Heisenberg and Fermi-Hubbard models with  $L = 32$ , respectively, using  $\sim 10^{6–7}$  iterations.

We benchmark the performance of the qMPS, qMERA, and global QC ansatz versus the dense MPS (DMRG) and dense MERA for the Heisenberg and Fermi-Hubbard models with  $L = 32$ . The key findings are as follows: (i) Comparing dense MPS with qMPS, we find that for an equivalent number of variational parameters, qMPS achieves lower energies than the dense MPS (see Figs. 7(a), (d)) in both the Heisenberg and Fermi-Hubbard models. (ii) Similarly, comparing dense MERA with qMERA, we find that for an equivalent number of variational parameters, qMERA achieves lower energies than

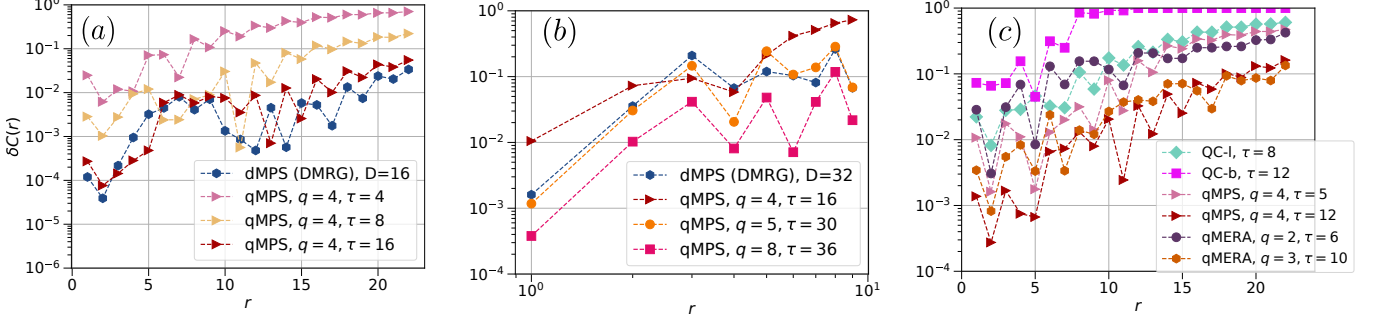


FIG. 8. (Color online) Relative error in the spin-spin correlation function as a function of distance  $r$ . (a), (c) are for the Heisenberg model, while (b) is for the Fermi-Hubbard model (both  $L = 32$ ). Both qMPS and qMERA use a local brick-work circuit (qMPS-b, qMERA-b). In (a), the qMPS with  $q = 4, \tau = 16$  has fewer parameters than the dMPS with  $D = 16$ , while in (b), the qMPS with  $q = 5, \tau = 30$  has fewer parameters than the dMPS with  $D = 32$ . In (c), the QC-I ansatz has a comparable numbers of parameters to the qMERA-b and qMPS-b with  $q = 2, \tau = 6$  and  $q = 4, \tau = 5$ , respectively. qMPS-b ( $q = 4, \tau = 12$ ) and qMERA-b ( $q = 3, \tau = 10$ ) have comparable numbers of variational parameters.

dense MERA. Taken together with the previous statement, this implies that the *appropriate quantum circuit tensor networks are more compact and expressive than their traditional dense counterparts* for these problems. (iii) Such expressiveness is not shared by the global brick-wall and ladder circuits (Figs. 7(b), (e)) which are consistently less expressive than the qMPS. (iv) qMPS is somewhat more expressive than qMERA (Figs. 7(c), (f)).

Empirically, we can also summarize the data by fitting the relative error to the inverse polynomial  $\delta E(n) \sim an^{-b}$ , where  $n$  is the number of variational parameters. As shown in Fig. 7 in the log-log plot, this form fits all the ansätze reasonably well, with some small systematic deviations, for example in the case of DMRG at larger  $n$ . A linear fit to the log-log data yields an estimate of  $a$  and  $b$ , as shown in Table I, where  $b$  gives the asymptotic scaling for large  $n$ . These results further support the findings above: in the large  $n$ -limit, the qMPS ansatz is the most expressive ansatz and outperforms the dense MPS, while qMERA outperforms the dense MERA, with both also outperforming the global brick-wall and ladder ansatz. We see that the brick-wall local circuit structure for qMPS yields a better overall performance than local ladder/MERA structures (see also Appendix A). The qMERA ansatz performs similarly to the dense MPS algorithm in both models with  $b_{\text{qMERA}} \approx b_{\text{dMPS}}$ . The ratio  $b_{\text{qMPS}}/b_{\text{qMERA}}$  and  $b_{\text{qMPS}}/b_{\text{dMPS}}$  is  $\sim 1.3$  in both models. Earlier studies of scale-invariant MERA and infinite MPS have found a similar ratio,  $b_{\text{MPS}}/b_{\text{MERA}} \sim 1.2$ <sup>37</sup>. Finally, depending on the model, either QC-b or QC-I performs better:  $b_{\text{QC-b}} < b_{\text{QC-I}}$  ( $b_{\text{QC-b}} > b_{\text{QC-I}}$ ) for the Heisenberg (Fermi-Hubbard) models, respectively.

## B. Correlation functions

We next study how faithfully the different ansätze capture correlation functions of the Heisenberg and Fermi-Hubbard models. We use the spin-spin correlation function, defined as  $\langle \vec{S}_0 \cdot \vec{S}_r \rangle - \langle \vec{S}_0^2 \rangle$  (Heisenberg and Fermi-Hubbard) as a repre-

sentative example.

In Fig. 8, we show errors in the correlation function  $\delta C(r)$  (relative to numerically exact data) for the various ansätze. In Fig. 8(a) (Heisenberg model), we see that qMPS-b with  $q = 4, \tau = 16$  produces the same algebraically decaying correlation function as a dense MPS with  $D = 16$  over the full distance range of  $r < 22$ , despite having fewer variational parameters. In Fig. 8(b) (Hubbard model), we similarly find that qMPS-b with  $q = 5, \tau = 30$  produces a similar quality correlation function to the dense MPS with  $D = 32$ , but again with fewer variational parameters. These results are consistent with the greater expressiveness of the quantum circuit tensor network relative to its dense counterpart.

In both models, we see that increasing either  $\tau$  or  $q$  leads to an improvement of the correlation function. However, neither is a dominant factor for convergence. For example, in the Heisenberg model, we find that using a qMPS-b with  $q = 5, \tau = 14$  provides a lower relative error compared to  $q = 4, \tau = 18$ , despite having fewer variational parameters; but a qMPS-b with  $q = 8, \tau = 4$  performs similarly to  $q = 4, \tau = 5$ , despite having a large number of variational parameters. Thus a balanced choice of  $q, \tau$  is needed to obtain the best result.

In Fig. 8(c), we show the qMERA-b, and QC-I correlation functions alongside the qMPS-b correlation functions. (We do not show the QC-b correlation functions which are generally worse than those from the above ansatz). One expects that qMPS-b will accurately reproduce short-range correlations (up to the MPS correlation length) while qMERA should perform better at long distances. Quantitatively, we find that qMPS-b ( $q = 4, \tau = 12$  and  $\delta E = 6 \times 10^{-5}$ ) indeed provides a lower relative error at short distances, while qMERA-b (with  $q = 3, \tau = 10$  and  $\delta E = 3 \times 10^{-4}$ ) with a similar number of variational parameters is more accurate at longer distances ( $r > 15$ ). In addition, qMPS with  $q = 4, \tau = 5$  outperforms QC-I with a similar number of parameters, especially at short distances. At long range, qMERA-b with  $q = 2, \tau = 6$  is clearly better than QC-I, while at short distances it is com-

parable. Overall, qMPS and qMERA thus appear to provide more faithful representations of the correlation functions than the general quantum circuit ansatz.

## V. CONCLUSIONS

In this work we studied the variational power of quantum circuit tensor networks, and in particular, quantum circuit matrix product states and the quantum circuit multi-scale entanglement renormalization ansatz, for representing the ground-states of quantum many-particle problems. As we argued, this is a problem where standard tensor networks excel, and is thus a high bar for quantum circuit tensor networks to meet. We found that quantum circuit tensor networks outperform other common quantum circuit ansatz, requiring far fewer parametrized gates for a given accuracy. In fact, they appear to be asymptotically even more expressive than the standard tensor networks, in terms of the number of parameters to converge to a comparable accuracy in the variational energy and correlation functions.

Although all simulations here were carried out classically, the scaling of the achieved accuracy as a function of the number of parameters suggests that the advantage in expressiveness displayed by quantum circuit tensor networks will persist into a regime where they can no longer be contracted efficiently classically. Assuming standard tensor networks are the best classical representation for these problems, the increasing compactness of the quantum circuit tensor networks relative to the competing classical ansatz in the high accu-

racy regime suggests a region of advantage in the representation of ground-states even in 1D systems. Of course to seize this potential advantage, one would also need to optimize circuit parameters in this classically-intractable regime. While the optimization heuristics discussed in this work successfully find accurate ground-states with a tractable number of optimization iterations, it remains to be seen whether this scaling persists in very large circuits. Perhaps more seriously, if the optimization is to be carried out on a quantum device, one may also need to account for large sampling overheads to resolve small gradients. However, the variational power of the quantum circuit tensor networks we have characterized provides new motivation to improve the optimization strategies for this class of circuit ansatz, both in the context of classical simulations, as well as on quantum architectures.

## ACKNOWLEDGMENTS

Primary funding for this work (RH, JG, GKC) was provided by the US Department of Energy, Office of Science, via DE-SC19374. GKC acknowledges additional support from the Simons Foundation via the Many-Electron Collaboration and via the Simons Investigator program. ACP was supported by the US NSF Convergence Accelerator Track C award 2040549. The numerical codes were implemented in the `quimb` library<sup>27</sup> which is freely available<sup>38</sup>. Development of the `quimb` library is supported in part by a gift from Amazon Web Services, Inc.

\* [haqshena@caltech.edu](mailto:haqshena@caltech.edu)

† [jgray@caltech.edu](mailto:jgray@caltech.edu)

‡ [garnetc@caltech.edu](mailto:garnetc@caltech.edu)

<sup>1</sup> Isaac H. Kim and Brian Swingle, “Robust entanglement renormalization on a noisy quantum computer,” (2017), [arXiv:1711.07500 \[quant-ph\]](https://arxiv.org/abs/1711.07500).

<sup>2</sup> Iris Cong, Soonwon Choi, and Mikhail D. Lukin, “Quantum convolutional neural networks,” *Nature Physics* **15**, 1273–1278 (2019).

<sup>3</sup> William Huggins, Piyush Patil, Bradley Mitchell, K Birgitta Whaley, and E Miles Stoudenmire, “Towards quantum machine learning with tensor networks,” *Quantum Science and Technology* **4**, 024001 (2019).

<sup>4</sup> Michael Foss-Feig, David Hayes, Joan M. Dreiling, Caroline Figgatt, John P. Gaebler, Steven A. Moses, Juan M. Pino, and Andrew C. Potter, “Holographic quantum algorithms for simulating correlated spin systems,” (2020), [arXiv:2005.03023 \[quant-ph\]](https://arxiv.org/abs/2005.03023).

<sup>5</sup> Bela Bauer, Sergey Bravyi, Mario Motta, and Garnet Kin-Lic Chan, “Quantum algorithms for quantum chemistry and quantum materials science,” *Chemical Reviews* **120**, 12685–12717 (2020), pMID: 33090772, <https://doi.org/10.1021/acs.chemrev.9b00829>.

<sup>6</sup> F. Barratt, James Dborin, Matthias Bal, Vid Stojovic, Frank Pollmann, and A. G. Green, “Parallel quantum simulation of large systems on small nisq computers,” *npj Quantum Information* **7**, 79 (2021).

<sup>7</sup> Michael Foss-Feig, Stephen Ragole, Andrew Potter, Joan Dreiling, Caroline Figgatt, John Gaebler, Alex Hall, Steven Moses, Juan Pino, Ben Spaun, *et al.*, “Entanglement from tensor networks on a trapped-ion qcd quantum computer,” arXiv preprint arXiv:2104.11235 (2021).

<sup>8</sup> Eli Chertkov, Justin Bohnet, David Francois, John Gaebler, Dan Gresh, Aaron Hankin, Kenny Lee, Ra’anan Tobey, David Hayes, Brian Neyenhuis, *et al.*, “Holographic dynamics simulations with a trapped ion quantum computer,” arXiv preprint arXiv:2105.09324 (2021).

<sup>9</sup> Alexey Uvarov, Jacob D. Biamonte, and Dmitry Yudin, “Variational quantum eigensolver for frustrated quantum systems,” *Phys. Rev. B* **102**, 075104 (2020).

<sup>10</sup> Sheng-Hsuan Lin, Rohit Dilip, Andrew G. Green, Adam Smith, and Frank Pollmann, “Real- and imaginary-time evolution with compressed quantum circuits,” *PRX Quantum* **2**, 010342 (2021).

<sup>11</sup> Lucas Slattery, Benjamin Villalonga, and Bryan K. Clark, “Unitary block optimization for variational quantum algorithms,” (2021), [arXiv:2102.08403 \[quant-ph\]](https://arxiv.org/abs/2102.08403).

<sup>12</sup> Reza Haghshenas, “Optimization schemes for unitary tensor-network circuit,” *Phys. Rev. Research* **3**, 023148 (2021).

<sup>13</sup> G. Vidal, “Class of quantum many-body states that can be efficiently simulated,” *Phys. Rev. Lett.* **101**, 110501 (2008).

<sup>14</sup> Ian Affleck, Tom Kennedy, Elliott H. Lieb, and Hal Tasaki, “Rigorous results on valence-bond ground states in antiferromagnets,” *Phys. Rev. Lett.* **59**, 799–802 (1987).

<sup>15</sup> F. Verstraete, M. M. Wolf, D. Perez-Garcia, and J. I. Cirac, “Criticality, the area law, and the computational power of projected entangled pair states,” *Phys. Rev. Lett.* **96**, 220601 (2006).

<sup>16</sup> F. Verstraete, V. Murg, and J.I. Cirac, “Matrix product states, projected entangled pair states, and variational renormalization group methods for quantum spin systems,” *Advances in Physics* **57**, 143–224 (2008), <http://dx.doi.org/10.1080/14789940801912366>.

<sup>17</sup> D. Perez-Garcia, F. Verstraete, M. M. Wolf, and J. I. Cirac, “Matrix product state representations,” *Quantum Info. Comput.* **7**, 401–430 (2007).

<sup>18</sup> Guifré Vidal, “Efficient classical simulation of slightly entangled quantum computations,” *Phys. Rev. Lett.* **91**, 147902 (2003).

<sup>19</sup> Steven R. White, “Density matrix formulation for quantum renormalization groups,” *Phys. Rev. Lett.* **69**, 2863–2866 (1992).

<sup>20</sup> Reza Haghshenas, Matthew J. O’Rourke, and Garnet Kin-Lic Chan, “Conversion of projected entangled pair states into a canonical form,” *Phys. Rev. B* **100**, 054404 (2019).

<sup>21</sup> Michael P. Zaletel and Frank Pollmann, “Isometric tensor network states in two dimensions,” *Phys. Rev. Lett.* **124**, 037201 (2020).

<sup>22</sup> C. Schön, K. Hammerer, M. M. Wolf, J. I. Cirac, and E. Solano, “Sequential generation of matrix-product states in cavity qed,” *Phys. Rev. A* **75**, 032311 (2007).

<sup>23</sup> G. Evenbly and G. Vidal, “Algorithms for entanglement renormalization,” *Phys. Rev. B* **79**, 144108 (2009).

<sup>24</sup> G. Evenbly and G. Vidal, “Tensor network states and geometry,” *Journal of Statistical Physics* **145**, 891–918 (2011).

<sup>25</sup> Empirically, we find that qMERA with local brick-wall and ladder circuits variationally behave very similarly, at least within the range of accessible qubits  $q$  and circuit depth  $\tau$  presented in this work.

<sup>26</sup> A further reduction in the number of parameters is possible by eliminating one parameter along the connected bonds, absorbing a rotational gate into adjacent gates, and also 6 parameters for two gates acting on top of each other. In our reported data, we have considered these reductions, which mainly change the scaling prefactor  $a$ , not the important exponent  $b$ .

<sup>27</sup> Johnnie Gray, “quimb: a python library for quantum information and many-body calculations,” *Journal of Open Source Software* **3**, 819 (2018).

<sup>28</sup> Johnnie Gray and Stefanos Kourtis, “Hyper-optimized tensor network contraction,” *Quantum* **5**, 410 (2021).

<sup>29</sup> Jorge Nocedal, “Updating quasi-newton matrices with limited storage,” *Mathematics of computation* **35**, 773–782 (1980).

<sup>30</sup> Jorge Nocedal and S. Wright, *Numerical Optimization* (Springer-Verlag New York, 2006).

<sup>31</sup> Jarrod R. McClean, Sergio Boixo, Vadim N. Smelyanskiy, Ryan Babbush, and Hartmut Neven, “Barren plateaus in quantum neural network training landscapes,” *Nature Communications* **9**, 4812 (2018).

<sup>32</sup> Edward Grant, Leonard Wossnig, Mateusz Ostaszewski, and Marcello Benedetti, “An initialization strategy for addressing barren plateaus in parametrized quantum circuits,” *Quantum* **3**, 214 (2019).

<sup>33</sup> Tyler Volkoff and Patrick J Coles, “Large gradients via correlation in random parameterized quantum circuits,” *Quantum Science and Technology* **6**, 025008 (2021).

<sup>34</sup> M. Cerezo, Akira Sone, Tyler Volkoff, Lukasz Cincio, and Patrick J. Coles, “Cost function dependent barren plateaus in shallow parametrized quantum circuits,” *Nature Communications* **12**, 1791 (2021).

<sup>35</sup> Chen Zhao and Xiao-Shan Gao, “Analyzing the barren plateau phenomenon in training quantum neural networks with the ZX-calculus,” *Quantum* **5**, 466 (2021).

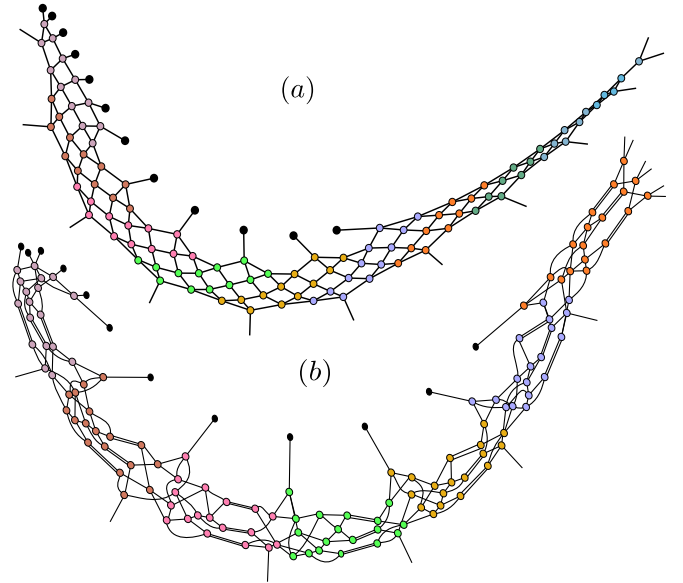


FIG. 9. (Color online) Schematic representation of a qMPS circuit with (a) ladder and (b) MERA internal local circuits, with local depth  $\tau = 2, 4$  and bond qubits  $q = 5, 6$ , respectively.

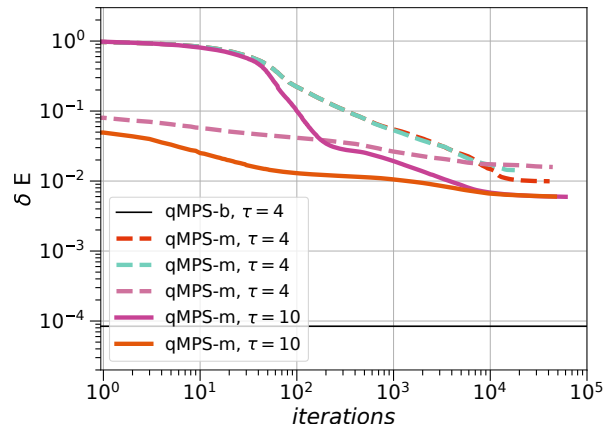


FIG. 10. (Color online) Comparison between qMPS with MERA and brick-wall local circuits. The solid and dashed lines represent two different initial starting states.

<sup>36</sup> Nicholas H Stair and Francesco A Evangelista, “Exploring hilbert space on a budget: Novel benchmark set and performance metric for testing electronic structure methods in the regime of strong correlation,” *The Journal of Chemical Physics* **153**, 104108 (2020).

<sup>37</sup> A. Avella and F. Mancini, *Strongly correlated systems : numerical methods*, Vol. 124 (Springer-Verlag Berlin Heidelberg, 2013).

<sup>38</sup> <https://github.com/jcmgray/quimb>.

## Appendix A: qMPS with MERA local circuits

We benchmark the accuracy of the qMPS-m ansatz by studying the relative error  $\delta E$  for the Heisenberg model  $\mathcal{H}_H$ .

In general, a systematic study of the ansatz is difficult as there are many controlling parameters:  $q, q_m, \tau$  where  $q_m$  is the number of bond qubits for the local MERA; and in addition, there is also the choice of the internal structure of the local MERA. To simplify things, we fix the number of bond qubits to  $q = 8$  and use a brick-wall structure for the MERA with  $q_m = 3$ . Empirically, we find that it is difficult to obtain converged results for qMPS-m as it easily gets stuck in local minima. Thus, for the reported data, two different initial states

were chosen, one random and one obtained from a smaller optimized circuit. In Fig. 10(a), we compare qMPS-m with qMPS-b for different  $\tau$ . We find that the qMPS-b with  $\tau = 4$  easily outperforms qMPS-m with  $\tau = 4$  (which has a larger number of variational parameters). We see that increasing  $\tau$  in qMPS-m from 4 to 10 only slightly improves the relative error, i.e. from  $9 \times 10^{-3}$  to  $6 \times 10^{-3}$ . Overall, the complexity of this circuit structure may require additional improvements in optimization strategy in order to realize its variational power.